ACS NANO

www.acsnano.org

ARTICLE

Near Degeneracy of Magnetic Phases in Two-Dimensional Chromium Telluride with Enhanced Perpendicular Magnetic Anisotropy

Amanda L. Coughlin, Dongyue Xie, Yue Yao, Xun Zhan, Qiang Chen, Heshan Hewa-Walpitage, Xiaohang Zhang, Hua Guo, Haidong Zhou, Jun Lou, Jian Wang, Yan S. Li, Herbert A. Fertig, and Shixiong Zhang*

Cite This: *ACS Nano* 2020, 14, 15256–15266

Read Online

ACCESS | Metrics & More | Article Recommendations | Supporting Information

ABSTRACT: The discovery of atomically thin van der Waals magnets (*e.g.*, CrI_3 and $Cr_2Ge_2Te_6$) has triggered a renaissance in the study of two-dimensional (2D) magnetism. Most of the 2D magnetic compounds discovered so far host only one single magnetic phase unless the system is at a phase boundary. In this work, we report the near degeneracy of magnetic phases in ultrathin chromium telluride (Cr_2Te_3) layers with strong perpendicular magnetic anisotropy highly desired for stabilizing 2D magnetic order. Single-crystalline Cr_2Te_3 nanoplates with a trigonal structure (space group $P\bar{3}1c$) were grown by chemical vapor deposition. The bulk magnetization measurements suggest a ferromagnetic (FM) order with an enhanced perpendicular magnetic anisotropy, as evidenced by a coercive field as large as ~14 kOe when the field is applied perpendicular to the basal plane of the thin nanoplates. Magneto-optical Kerr effect studies confirm the intrinsic ferromagnetism and characterize the magnetic ordering temperature of individual nanoplates. First-principles density functional theory calculations suggest the near degeneracy of magnetic orderings with a continuously varying canting from the *c*-axis FM due to their comparable energy scales, explaining the zero-field kink observed in the magnetic hysteresis loops. Our work highlights Cr_2Te_3 as a promising 2D Ising system to study magnetic phase coexistence and switches for ultracompact information storage and processing.

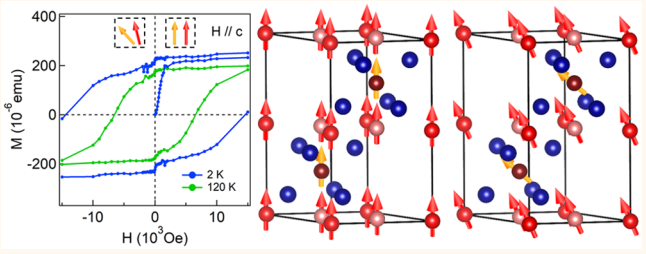

KEYWORDS: *2D magnets, chromium telluride, perpendicular magnetic anisotropy, canted ferromagnetic order, phase degeneracy*

Two-dimensional (2D) magnetism has a long history from the theoretical prediction of monolayer Ising magnets in 1944[1] and experimental realization of ferromagnetic metal thin films in the 1980s and 1990s[2−5] to the recent discovery of van der Waals (vdW) ferromagnets (*e.g.*, CrI_3 and $Cr_2Ge_2Te_6$).[6,7] The atomically thin vdW magnets provide an excellent platform to examine well-established theories of 2D magnetism[1,8−10] and to search for exotic quantum phases.[11] Furthermore, they hold great promise for device applications with enhanced functionalities as they can be readily stacked into heterostructures and their magnetic properties are highly tunable by external stimulus (*e.g.*, strain, electric field).[12−14] For example, giant tunneling magnetoresistance has been observed at low temperatures in some unconventional magnetic tunnel junctions in which ultrathin CrI_3 acts as a spin-filter tunnel barrier between two nonmagnetic vdW electrodes.[15−18] There has also been success in engineering and manipulating the spin and valley pseudospin in CrI_3/WSe_2 heterostructures by applying magnetic fields[19] or optically generated pseudomagnetic fields,[20] as well as the ordered magnetic phases in CrI_3 and $Cr_2Ge_2Te_6$ through external electric fields and electrostatic doping.[21,22]

In parallel to the immense efforts on devices, there is great interest in discovering 2D magnetic compounds with high magnetic ordering temperatures and different magnetic phases.[23−52] Room-temperature ferromagnetism has been realized in molecular beam epitaxy (MBE) grown $MnSe_x$ monolayer films[31] and mechanically exfoliated thin Fe_3GeTe_2 flakes under ionic gating.[35] Beyond vdW magnets, other layered non-vdW materials, such as hematene α-Fe_2O_3 layers,

Received: July 4, 2020
Accepted: October 22, 2020
Published: October 30, 2020

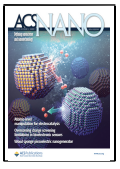

https://dx.doi.org/10.1021/acsnano.0c05534
ACS Nano 2020, 14, 15256−15266

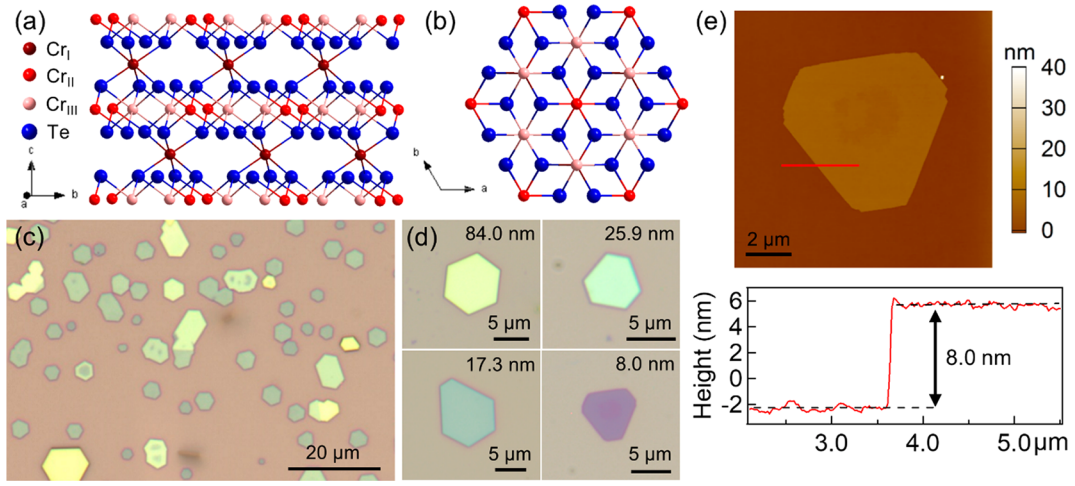

Figure 1. Crystal structure of Cr_2Te_3 (space group: $P\bar{3}1c$) shown from the (a) side view and (b) top view. (c) Optical image of a representative area on the growth substrate with nanoplates of various contrasts and (d) corresponding thicknesses. (e) AFM image with the corresponding height profile of an 8 nm Cr_2Te_3 nanoplate.

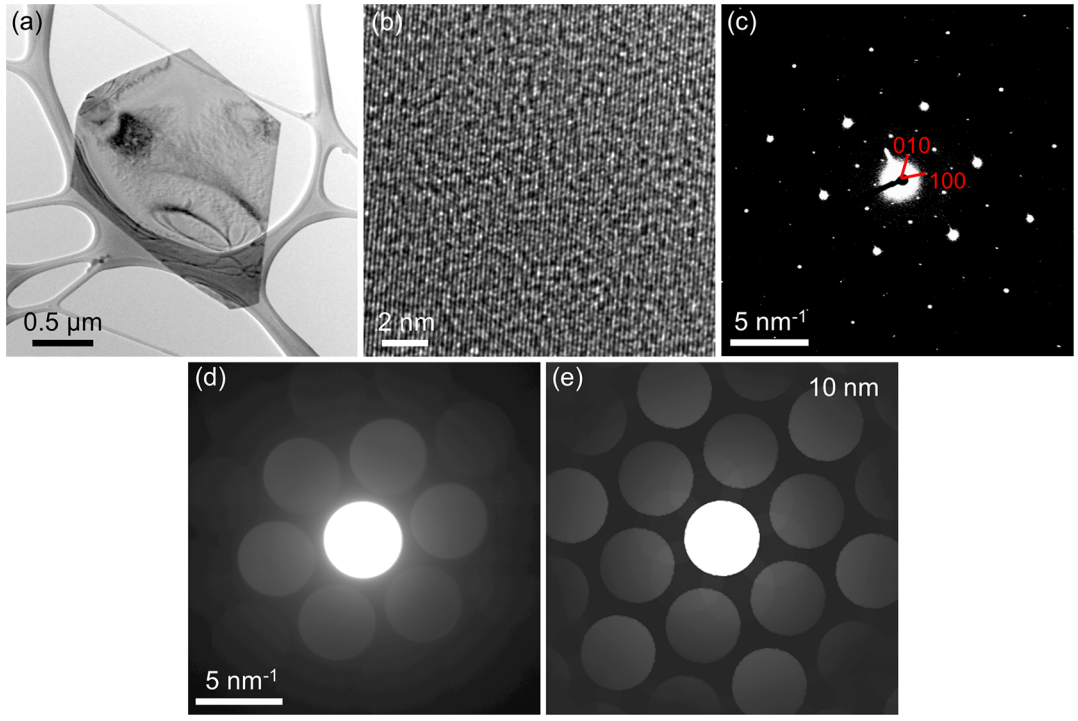

Figure 2. (a) Bright field TEM image, (b) HRTEM image, (c) SAED pattern, and (d) CBED pattern taken along the ⟨001⟩ zone axis of a Cr_2Te_3 nanoplate. (e) Simulated CBED pattern of a 10 nm thick Cr_2Te_3 of space group $P\bar{3}1c$.

have been successfully exfoliated from their bulk crystals, in which magnetic order at room temperature has been observed.[53] Likewise, room-temperature magnetic order has been realized in chemical vapor deposition (CVD)-grown ultrathin ε-Fe_2O_3 nanoplates which exhibit vdW-like properties, enabling the simple transfer and fabrication of non-vdW heterostructures for spintronic applications.[54] However, in spite of the tremendous success in enhancing the magnetic ordering temperature, the 2D magnetic compounds reported so far only host a single magnetic phase unless the system is at a phase boundary, as found in CrI_3 at an intermediate thickness.[55,56]

Here we report on intrinsically coexisting magnetic phases in ultrathin crystals of Cr_2Te_3, a layered chromium telluride compound with strong perpendicular anisotropy. Although a non-vdW material, single-crystalline Cr_2Te_3 nanoplates down to ∼7 unit cells thick were successfully grown by CVD, with the vdW-like bonding between the substrate and nanoplates facilitating easy transfer *via* the stamping method. Bulk magnetization measurements revealed a strong magnetic anisotropy with the easy axis perpendicular to the basal plane. The perpendicular magnetic anisotropy is enhanced in a thin nanoplate sample where a coercive field as large as ∼14 kOe is observed. Magneto-optical Kerr effect (MOKE) measurements confirm the intrinsic ferromagnetism and determine the magnetic ordering temperature of individual nanoplates. First-principles density functional theory (DFT) calculations suggest the near degeneracy of *c*-axis ferromag-

https://dx.doi.org/10.1021/acsnano.0c05534
ACS Nano 2020, 14, 15256−15266

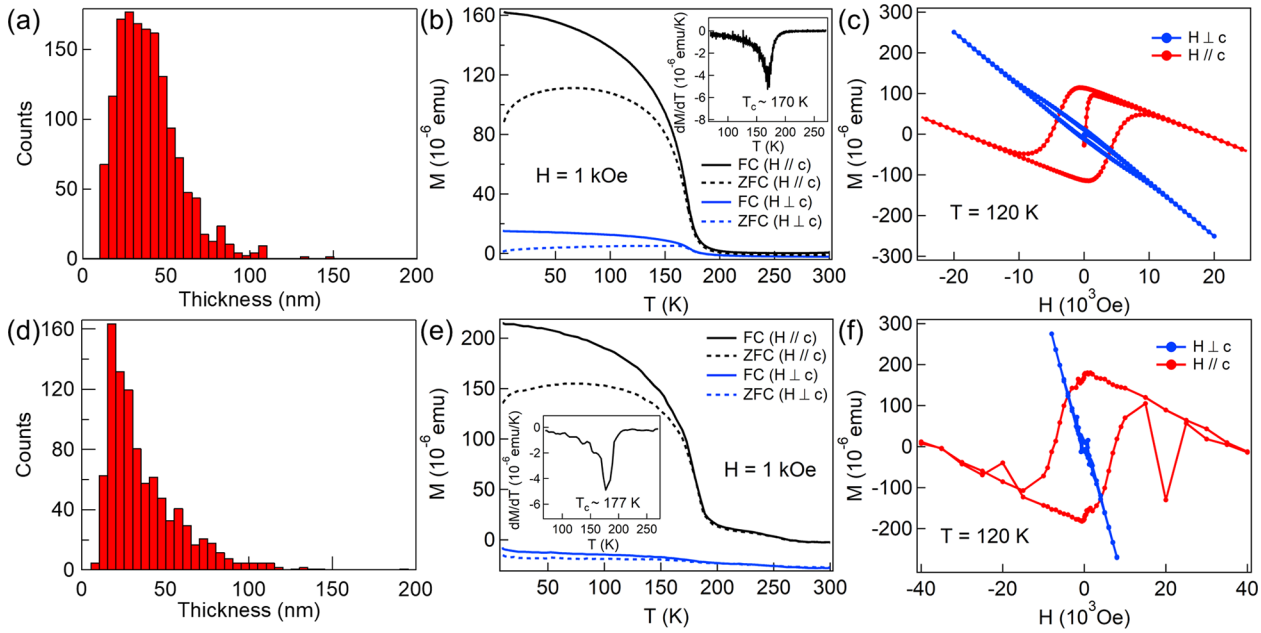

Figure 3. Histograms showing the thicknesses of nanoplates for the (a) thick and (d) thin samples. (b, e) FC (solid) and ZFC (dashed) $M-T$ curves of the thick and thin samples with the magnetic field both parallel (black) and perpendicular (blue) to the c-axis with an applied field of 1 kOe. The insets are the derivative of M with respect to T to derive the T_c of Cr_2Te_3. (c, f) $M-H$ curves of the thick and thin samples with the magnetic field aligned perpendicular (blue) and parallel (red) to the c-axis at T = 120 K. The negative magnetization in the $H \perp c$ cases are due to the contribution from the diamagnetic SiO_2/Si growth substrate which dominates over the weak net magnetization perpendicular to the easy axis.

netic and canted ferromagnetic phases, explaining the zero-field kink observed in the magnetic hysteresis. Our work demonstrates Cr_2Te_3 as a promising platform to study the magnetic phase coexistence and magnetic switches in 2D systems.

RESULTS AND DISCUSSIONS

Cr_2Te_3 belongs to the trigonal crystal system and has a hexagonal lattice system described by the space group $P\bar{3}1c$ with lattice parameters a = 6.814 Å and c = 12.073 Å at room temperature.[57] As shown in Figure 1(a) and (b), the unit cell contains alternating layers of Cr and Te atoms and has Cr_I vacancies in every second metal layer. The Cr_I atoms in the partially occupied layers are sandwiched between the Cr_{III} layers and have no close-by neighbors in the $a-b$ plane, whereas the Cr_{II} and Cr_{III} atoms make up the fully occupied metal layers.[58] The CVD-grown, individual Cr_2Te_3 nanoplates typically have a hexagonal shape [Figure 1(c)], resembling the hexagonal lattice in the (001) plane and thereby indicating high crystalline quality. They have varied colors under an optical microscope, and the optical contrast is directly related to the thickness of the nanoplates. As shown in Figure 1(d), the thickest nanoplates have a yellow contrast, and as thickness decreases, the optical contrast changes through three main transitions: to green, blue, and finally purple. As each respective color deepens, the nanoplate thickness decreases (*i.e.*, light purple nanoplates are thicker than darker purple ones). The thinnest nanoplates were grown down to 8 nm (*i.e.*, ~7 unit cells), as shown in Figure 1(d) and the atomic force microscopy (AFM) measurement in Figure 1(e). Like vdW materials, Cr_2Te_3 nanoplates can easily be transferred from the rigid SiO_2/Si growth substrate simply by stamping onto a clean substrate [Figure S2]. The weak vdW-like bonding between the nanoplates and the growth substrate could be taken advantage of in future fabrication of heterostructure devices.

Cr_2Te_3 shares a similar structure with many other chromium telluride compounds (*i.e.*, Cr_3Te_4, Cr_5Te_8, *etc.*).[57−61] Depending on the Cr deficiency in the second metal layers, the magnetic ordering temperature of the compound varies between 170 and 340 K.[57,58,62] Therefore, it is important to carefully characterize the crystal structure of the nanoplates to ensure the correct attribution of the magnetic properties. The c-lattice constant of the various chromium tellurides varies only slightly between the compounds,[57,58,60−62] making it challenging to distinguish the different phases by X-ray diffraction characterization of d-spacing in the c-direction [Figure S3]. In contrast, the a-lattice constant varies considerably among different compounds. We therefore performed transmission electron microscopy (TEM) studies along the [001] zone axis to characterize the lattice structure in the (001) plane (*i.e.*, the $a-b$ plane) to verify the Cr_2Te_3 phase. Figure 2 shows the bright field, high-resolution TEM (HRTEM) images, selected-area electron diffraction (SAED) pattern, and convergent-beam electron diffraction (CBED) pattern of a representative Cr_2Te_3 nanoplate. The low-magnification image is nearly transparent, indicating the nanoplate is ultrathin. The single-crystalline nature of the nanoplate is evidenced by the SAED, which can be well indexed by the Cr_2Te_3 trigonal phase with a space group of $P\bar{3}1c$. The diffraction vector $k\{100\}$ was determined to be 1.7 nm^{-1}, consistent with the lattice constant a = 0.6814 nm.[57] These {100} diffraction spots are the characteristic spots distinguishing Cr_2Te_3 from other phases, as shown in Figures S4 and S5. We indeed ruled out the existence of other phases of chromium tellurides by comparing the experimental data to simulations of other diffraction patterns taken along the [001] zone axis (Figure S5). We note that while cross-sectional TEM is often used to characterize

https://dx.doi.org/10.1021/acsnano.0c05534
ACS Nano 2020, 14, 15256−15266

epitaxial thin film samples, such a study is very challenging for nanoplates/nanosheets that are weakly bounded to the substrate because they can be easily damaged during the TEM sample preparation. Instead, top-view TEM has been widely used to demonstrate high-quality single crystallinity in 2D nanosheets/nanoplates.[63−65] The stoichiometric ratio of Te:Cr was determined from TEM-EDX as approximately 1.43 (Figure S6). Given the EDX is a semiquantitative characterization tool, the measured Te:Cr ratio is sufficiently close to the stoichiometric value of Cr_2Te_3. Furthermore, the TEM-EDX mapping of Cr and Te demonstrate the uniform distribution of the elements throughout the nanoplate (Figure S6). From the TEM-EDX stoichiometry, together with the analysis of the diffraction patterns, we conclude that the sample is indeed Cr_2Te_3. The HRTEM image shows clear lattice fringes, further confirming the high crystal quality. An amorphous background was observed and should be attributed to the surface oxidation occurring commonly in many tellurides upon prolonged exposure to air.[66−68] The CBED pattern is in good agreement with the simulated pattern of trigonal Cr_2Te_3 with a thickness of ∼10 nm, as shown in Figure 2(d) and (e), respectively.

Magnetization measurements of the Cr_2Te_3 nanoplates suggest ferromagnetic order with enhanced perpendicular magnetic anisotropy. The measurements were taken on two samples of different thicknesses referred to as the "thick" sample and the "thin" sample. The maximum number of nanoplate thicknesses ranges between ∼25−30 nm and 15−20 nm for the thick and thin samples, respectively, as shown in the histograms in Figure 3(a) and (d), which have a bin width of 5 nm. While surface oxidation commonly observed in metal tellurides can indeed occur on the surface [Figure 2(b)], a previous report studied the impact of surface oxidation on the magnetic properties *via* X-ray magnetic circular dichroism and found the surface chromium oxide is most likely antiferromagnetic Cr_2O_3, which does not add to the observed ferromagnetic signal.[69] The total magnetization would decrease as the surface layer is transformed from ferromagnetic Cr_2Te_3 to antiferromagnetic Cr_2O_3 due to surface oxidation. To avoid this effect, we have minimized the samples' exposure time in air as described in the Supporting Information. Additionally, the samples were handled only with plastic tweezers to avoid possible magnetic contamination.[70] Therefore, the magnetic studies below probe the intrinsic properties of the Cr_2Te_3 nanoplates. Magnetization measurements as a function of temperature ($M-T$) with the magnetic field H parallel ($H \parallel c$) and perpendicular ($H \perp c$) to the c-axis for both field-cooling (FC) and zero-field-cooling (ZFC) were performed on the thick and thin samples with H = 1 kOe, as shown in Figure 3(b) and (e), respectively. The $M-T$ data demonstrate a paramagnetic to ferromagnetic transition below the Curie temperature, T_c. From the first-order derivative of $M-T$, the T_c is determined to be ∼170 K for the thick sample and ∼177 K for the thin sample, consistent with the T_c range reported in bulk crystals and thin films.[71−73] Since the magnetization measurement was performed on a bulk of nanoplates, the T_c determined here is an average value over those individual nanoplates. For both samples, the magnetization is much greater for $H \parallel c$ than $H \perp c$, indicating the c-axis is the magnetic easy axis and hence a perpendicular magnetic anisotropy (*i.e.*, perpendicular to the basal plane).

The ferromagnetism and perpendicular magnetic anisotropy are further confirmed by the magnetic field dependent magnetization ($M-H$) measurements. As shown in Figure 3(c) and (f), both samples yield large magnetic hysteresis loops when $H \parallel c$ and much smaller loops when $H \perp c$, again suggesting that the magnetic easy axis is along the c-axis. The negative slope of the $M-H$ at high fields is due to the diamagnetic background from the substrate. By subtracting this background (Supporting Information), we determined the temperature-dependent coercive field H_c of both samples [Figure S10]. Notably, the magnetic anisotropy is more dramatic in the thin sample. The thin sample has the largest coercive field for $H \parallel c$ (∼14 kOe at 2 K, ∼6.6 kOe at 120 K). The thick sample's H_c, when $H \parallel c$, at 3 and 120 K are ∼10 and ∼4.3 kOe, respectively. The coercive fields of both samples for $H \parallel c$ are higher than the H_c(2 K) ≈ 6.5 kOe[74] and H_c(3 K) = 6.0 kOe[69] reported in the MBE-grown thin films with a $T_c \approx$ 180−183 K. They are also significantly larger than the H_c(2 K) ≈ 2.2 kOe very recently reported in thin nanoflakes grown *via* CVD,[75] which shows weak anisotropy but has a transition temperature well above the reported $T_c \approx$ 180 K for bulk Cr_2Te_3.

The magnetic anisotropy constant K can be estimated using $|K| = \frac{1}{2}H_{sat}M_{sat}$[76] (or $\approx H_cM_{sat.}$),[77] where H_{sat} (H_c) is the saturation field (coercive field) at low temperatures and M_{sat} is the saturation magnetization. Using the M_{sat} of 2.48 μ_B/Cr,[78] $|K|$ is estimated to be ∼4−5 × 10^5 J m^{-3} for the thin Cr_2Te_3 sample. This anisotropy constant is larger than the experimental anisotropy constant for other 2D ferromagnetic materials such as $Cr_2Ge_2Te_6$[79] and CrI_3,[80] with values of ∼1.3 × 10^4 and ∼3 × 10^5 J m^{-3} at 5 K, respectively. In general, magnetic anisotropy comes from different sources, including magnetocrystalline anisotropy due to the crystal structure and spin−orbit coupling, shape anisotropy resulting from long-range dipolar interactions and demagnetization fields, and surface anisotropy associated with the breaking of symmetry at the surface or interfaces.[81] While the magnetocrystalline anisotropy is intrinsic to the material itself and the shape anisotropy depends on the shape of the material, the surface anisotropy is thickness dependent. The leading term in the anisotropy energy is given by $E = KV\cos^2\theta$, where V is the volume, θ is the angle between the magnetization M and the surface normal, and K is the anisotropy constant given by $K = K_{shape} + K_{m.c.} + n\frac{K_{surf}}{t}$.[82] Here K_{shape} is the shape anisotropy term, $K_{m.c.}$ is the magnetocrystalline anisotropy, n is the number of interfaces (n = 1 for structures that are not multilayered), K_{surf} is the surface anisotropy, and t is the thickness of the film.[83] In bulk Cr_2Te_3, it has been shown that the easy axis is along the c-axis, which means K should be negative, as well as the $K_{m.c.}$ term. K_{shape} is positive because the demagnetization fields favor an in-plane magnetization. Since the perpendicular anisotropy is enhanced in nanoplates in comparison with the bulk, the K_{surf} term is negative and the $\frac{K_{surf}}{t}$ term becomes more negative with decreasing thickness. As this term becomes more negative, it dominates over the shape anisotropy term and forces the easy axis to be along the c-axis, ultimately enhancing the anisotropy constant, as observed in some elemental metal thin films.[84−86]

It is important to note that the strong perpendicular anisotropy observed here is the key to stabilizing the magnetic order in the 2D limit.[6,87] Indeed, as described in the Mermin−Wagner−Hohenberg theorem, long-range magnetic order is prohibited in 2D isotropic Heisenberg systems with short-

https://dx.doi.org/10.1021/acsnano.0c05534
ACS Nano 2020, 14, 15256−15266

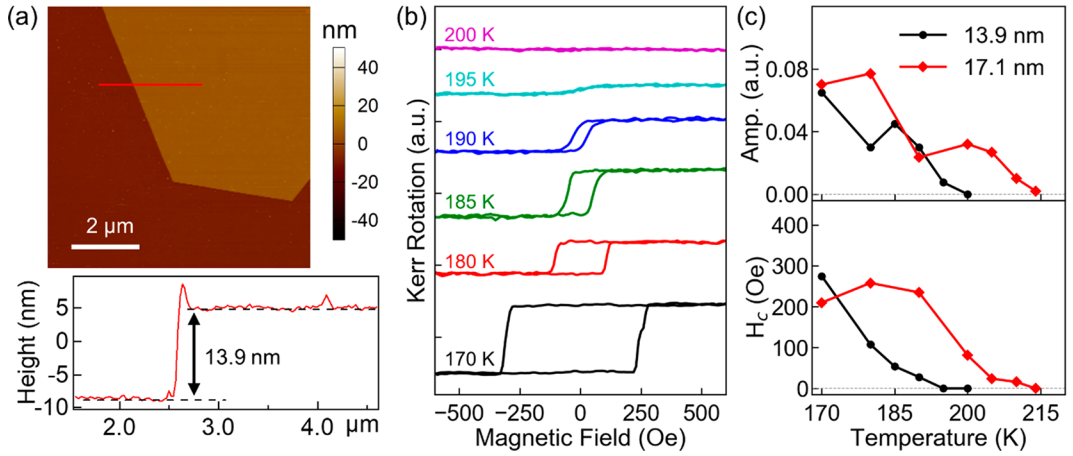

Figure 4. (a) AFM image and height profile of a nanoplate measured by MOKE. (b) MOKE hysteresis loops after background subtraction taken on the nanoplate shown in (a). (c) Amplitude of the Kerr rotation (upper panel) and the coercive field (lower panel) as a function of temperature for two nanoplates with different thicknesses.

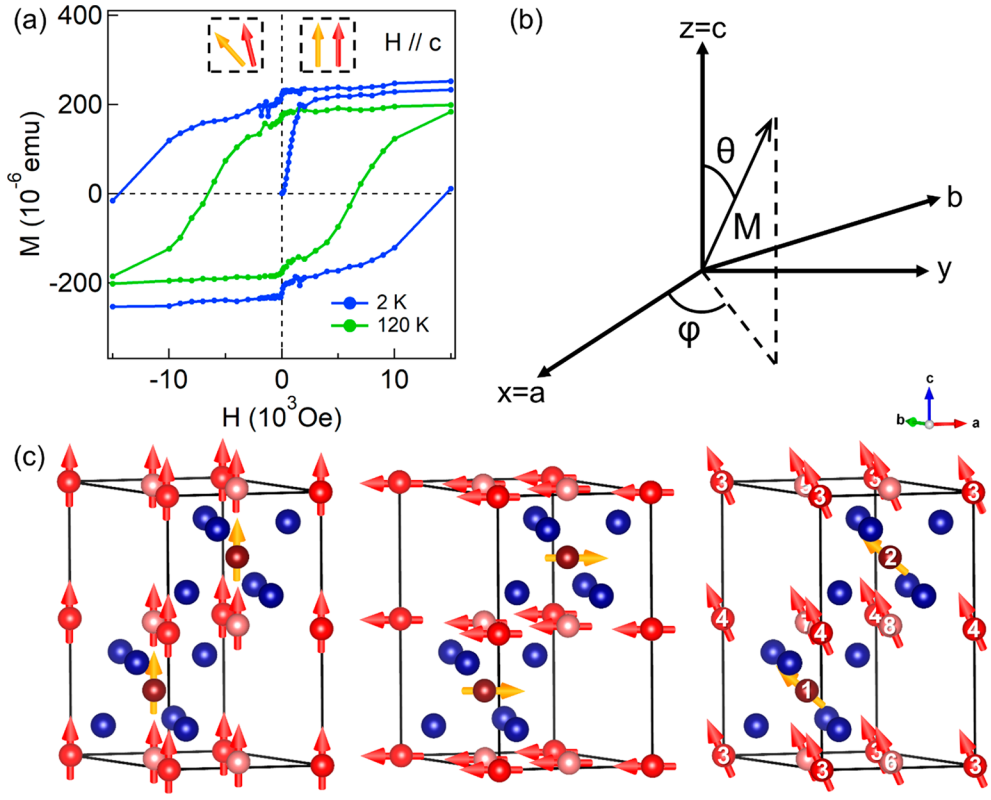

Figure 5. (a) Magnetization *versus* magnetic field of the thin sample after background subtraction. (b) ***M*** vector in spherical coordinates. (c) Schematics of the three different magnetic phases: *c*-axis FM order (left panel), FIM order (middle panel), and canted FM order (right panel).

range interactions due to strong thermal fluctuations.[10] The effect of thermal fluctuations can, however, be suppressed by magnetic anisotropy, which opens a gap in the spin wave spectrum. The observed perpendicular anisotropy suggests that the 2D Cr_2Te_3 contains an Ising-like magnetic order.

Beyond bulk magnetization studies, we performed MOKE measurements to characterize the magnetic ordering temperature T_c of individual Cr_2Te_3 nanoplates. The external magnetic field was applied perpendicular to the surface of the nanoplate (*i.e.*, along the *c*-axis), and the Kerr rotation measures mostly out-of-plane magnetization (Supporting Information). Figure 4(a) shows an AFM image of a nanoplate about 10 μm laterally and 13.9 nm thick from the depth profile. Because the field in the MOKE measurement is limited to ±600 Oe, we present only the MOKE loops at 170 K and above where the full major hysteresis loops are captured [Figure 4(b)]. The MOKE loops at 180 K have a coercive field of ∼100−260 Oe, agreeing with the coercive field of ∼100 Oe in bulk measurement hysteresis loops at 180 K of samples with similar thickness [Figure S10]. A small variation in coercive field is expected because the bulk measurement measures many nanoplates across a range of thicknesses at once, while MOKE

https://dx.doi.org/10.1021/acsnano.0c05534
ACS Nano 2020, 14, 15256−15266

Table 1. Initial and Calculated Magnetic Moment M, Polar Angle θ, and Azimuthal Angle φ of the Cr Moments in the Canted-FM State[a]

		Cr_I		Cr_{II}		Cr_{III}			
Cr site		1	2	3	4	5	6	7	8
initial state	M (μ_B)	3	3	3	3	3	3	3	3
	θ (deg)	90	90	0	0	0	0	0	0
	φ (deg)	0	0	/	/	/	/	/	/
final state	M (μ_B)	3.28	3.28	3.21	3.21	3.14	3.14	3.14	3.14
	θ (deg)	45.93	45.91	20.57	20.56	16.87	16.87	16.83	16.83
	φ (deg)	0.02	0.02	−4.22	4.28	7.95	7.70	−7.91	−7.59

[a]The calculated energy is −122.59822 eV/u.c.

only measures a single nanoplate of one specific thickness. As the temperature increases, both the magnitude of the Kerr rotation and the coercive field decrease, and the MOKE loop turns into a flat line at 200 K. The T_c is hence estimated based on the hysteresis loop to be about 195 K (this value can be slightly different from the ones determined from the dM/dT because of the different methods). MOKE measurements on a thicker nanoplate (17.1 nm) show a higher T_c of ∼210 K [Figure 4(c)]. The variation in T_c could be due to the difference in thickness or stoichiometry, or both. Indeed, the T_c of the chromium telluride family of compounds has a strong dependence on the stoichiometry, and a recent study of single-crystal samples shows a highly tunable T_c of up to ∼300 K with an increase of the Cr content.[88] Future studies decoupling the impact of thickness and stoichiometry would be essential to understand their relative influence on the T_c of 2D chromium telluride nanoplates.

Lastly, we discuss the possible magnetic structures of Cr_2Te_3 below T_c. Previous neutron scattering studies of a polycrystalline sample suggested a ferromagnetic (FM) structure, in which all of the Cr moments were thought to be aligned along the c-axis;[57] on the other hand, a similar study of single-crystal samples indicated a ferrimagnetic (FIM) structure where the magnetic moments in the partially occupied layers (*i.e.*, Cr_I) are antiferromagnetically aligned with the ones in the fully occupied layers (*i.e.*, Cr_{II} and Cr_{III}).[59] In both cases, the z-components of the moments in the fully occupied layers are slightly smaller than the spin-only Cr moments (*i.e.*, 3 μ_B), while the ones in the partially occupied layers have significantly smaller values. A closer examination of our M−H curves (after background subtraction) points to an unusual feature that cannot be explained by the simple FM or FIM picture. As seen in the background-subtracted M−H curves of the thin sample in Figure 5(a), a kink appears near the zero field in the magnetic hysteresis loops, as well as in the M−H curves of the thicker sample [Figure S11]. A similar kink with varied strengths was reported in some Cr_2Te_3 nanorods grown *via* an organic-solution-phase method,[77] as well as in Cr_2Te_3 thin films grown *via* MBE.[69] The kink is unlikely to be due to the variation in nanoplate thicknesses: (1) Our M−H data were taken over a range of thicknesses, so one would expect a smooth drop of magnetization in contrast to a sudden decrease (*i.e.*, a kink) in magnetization as a result of thickness variation; and (2) the films that show a similar feature have a uniform thickness.[69] To understand the experimental results, we carried out DFT calculations of various magnetic structures with the Vienna *Ab Initio* Simulation Package (VASP).[89] In this study, the generalized gradient approximation (GGA) approach was employed,[90] with the pseudopotentials generated using the projected augmented wave (PAW) method.[91] The exchange−correlation density functional is that of Perdew−Burke−Ernzerhof (PBE).[92] The HSE06 functional was used to perform screened hybrid functional calculations.[93,94] More calculation details are provided in the Methods section and the Supporting Information.

We started with the two simplest magnetic states, *i.e.*, the FM and FIM [Figure 5(c)]. The calculated energy of the FM state is 0.42 eV/unit cell (u.c.) lower than that of the FIM, suggesting that the latter is not an energetically favorable state. Since magnetic anisotropy is the key to stabilizing 2D magnetic order, we further computed the magnetocrystalline anisotropy constant (K_{cal}) for each magnetic structure, where the K_{cal} is defined as the energy difference per volume between the magnetic structures with magnetic moments along the c-axis (*i.e.*, [001]) and along the a-axis (*i.e.*, [100]), *i.e.*, $K_{cal.} = E_{[001]} - E_{[100]}$. The K_{cal} are found to be -5.3×10^6 J/m^3 (-1.6×10^{-2} eV/u.c.) and 1.9×10^6 J/m^3 (6×10^{-3} eV/u.c.) for the FM state and the FIM state, respectively. Therefore, the c-axis is the easy axis for the FM state but the hard axis for the FIM state. Given the observed perpendicular magnetic anisotropy, it is reasonable to rule out the possibility of an FIM ground state, which also has a higher energy than the FM state in our calculations. The calculated K_{cal} is about 1 order of magnitude higher than the value that is estimated from the M−H measurement. Such large differences have also been observed in some other 2D magnetic materials, *e.g.*, in $Cr_2Ge_2Te_6$.[79,95,96] The discrepancy likely has several sources. For example, the DFT calculations were performed at 0 K, while the experimental data were collected at higher temperatures. In addition to the effects of thermal fluctuations, quantum fluctuations would decrease the magnetic anisotropy constant from the DFT estimate even at zero temperature. Additionally, the magnetic properties of chromium telluride have a strong dependence on the Te:Cr stoichiometric ratio, which may not be exactly 1.5 as the DFT calculation assumes.

The Cr moments in the FM state calculated are 3.47 μ_B, 3.38 μ_B, and 3.35 μ_B for Cr_I, Cr_{II}, and Cr_{III}, respectively. These calculated values are close to previous local density approximation + U results[78] but are higher than the values extracted from neutron scattering measurements. To resolve this inconsistency, we further performed noncollinear self-consistent calculations without fixing the relative orientation of the magnetic moments. In this calculation, we started with an initial configuration where the moments in the fully occupied layers (Cr_{II} and Cr_{III}) point along the c-axis (or the z-axis), while those in the partially occupied layers (Cr_I) are in the a−b plane (or the x−y plane). This configuration was chosen because the neutron scattering results show the z-components of the moments in the fully occupied layers to be much larger than those in the partially occupied layers. In this noncollinear

https://dx.doi.org/10.1021/acsnano.0c05534
ACS Nano 2020, 14, 15256−15266

calculation, the spinor wave functions were rotated from their initial orientation and the electronic density was optimized in each iteration. The magnitude M, polar angle θ, and azimuthal angle φ of the Cr moments in the lowest energy state are listed in Table 1. All the Cr moments are canted with respect to the c-axis, leading to a decreased z-component. We therefore call this state a canted-FM. The energy of the canted-FM is negligibly lower (by 4×10^{-4} eV/Cr) than the c-axis FM calculated using the same method [Table S1]. The polar/canting angle θ is ∼46° for the Cr_I in the partially occupied layers, while it is only 17−21° for the fully occupied layers. Therefore, the z-moment is smaller in the former than in the latter, qualitatively consistent with the neutron scattering results. It is worth noting that even if the initial z-components of the moments in the two layers (*i.e.*, the partially and fully occupied layers) are set to be antiparallel, they become parallel in the final state [Table S2]. Thus, it is reasonable to believe that the exchange coupling between the two layers is weakly ferromagnetic.

Furthermore, the two Cr_I moments are ferromagnetically coupled in the $x-y$ plane, which is likely to be an isotropic plane. Indeed, when the two Cr_I atoms are initially set to be both along the a-axis, their projections in the $x-y$ plane stay in the same direction [Table 1]; the azimuthal angle φ of the two Cr_I atoms becomes nearly the same (∼60°) in the final state even when they are initially set to be 0° (*i.e.*, along a-axis) and 120° (*i.e.*, along b-axis), respectively [Table S3]. The energies of these two final states are very close (with a negligible difference of 8×10^{-5} eV/Cr). We therefore believe that the $x-y$ plane is likely to be isotropic. Presuming the ground state energy is independent of the orientation of the spins in the $x-y$ plane, this state hosts, in addition to an Ising order parameter, a broken $U(1)$ symmetry, characterized by the azimuthal angle φ. Our calculations indicate that the in-plane component of the magnetic moment in each unit cell is small compared to the c-axis moment. This suggests the system has two ordering temperature scales, one high, at which the component of magnetization along the c-axis sets in, and one low, at which order in the $x-y$ plane sets in. Presuming the latter temperature is below that of the neutron scattering studies, this can explain the absence of ordered x- and y-components in them even in bulk crystals.

To study how the system evolves from the c-axis FM into a canted FM, we performed self-consistent calculations in which the initial moments were only slightly canted. As shown in Table S4, the final state arrived at has a canting angle that is nearly the same as the initial state. Interestingly, the changes in energy over a range of canting angles are extremely small, compared to, for example, the difference in energy between the FM and FIM states. This suggests that the energy surface as a function of the canting angle θ has a very small curvature, making the precise arrangement of spins in the lowest energy canted state difficult to locate. This behavior, however, offers an explanation for the kink near zero field in the magnetic hysteresis loop [Figure 5(a)]: with application of an external magnetic field, the canting angle will evolve rapidly such that the total magnetic moment in each unit cell moves toward alignment with the c-axis. Conversely, when sweeping toward zero field in a hysteresis loop, the magnetization will drop rapidly very close to a vanishing applied field as the canting angle sweeps through a continuum of states with only a small energy dispersion in the field's absence.

CONCLUSIONS

In summary, we have synthesized single-crystalline Cr_2Te_3 nanoplates with their thicknesses down to ∼7 unit cells by CVD and have studied their magnetic properties *via* bulk magnetization and MOKE measurements, in conjunction with DFT calculations. The bulk magnetization measurements suggested FM order with an enhanced perpendicular magnetic anisotropy, as evidenced by a coercive field as large as ∼14 kOe when the field is applied perpendicular to the basal plane. Magneto-optical Kerr effect studies confirm the intrinsic ferromagnetism and characterize the magnetic ordering temperature of individual nanoplates, highlighting the importance of decoupling the influence of thickness and stoichiometry. First-principles DFT calculations suggest the near degeneracy of magnetic orderings with a continuously varying canting from the c-axis FM because of their comparable energy scales. The field dependence arising from this weak energy variation may qualitatively explain the zero-field kink observed in the magnetic hysteresis loops. In this context, it is worth mentioning that a large topological Hall effect has recently been reported in Cr_2Te_3 embedded with Bi atoms[97] or coupled with Bi_2Te_3,[98] indicating the existence of magnetic skyrmions, a topologically nontrivial vortex spin configuration. The "continuous" spin-canting in the thin layers of undoped Cr_2Te_3 observed in this work may provide insight into the nature of these skyrmions, which offer opportunities for ultracompact information storage and processing applications based on spintronic devices.

METHODS

Experimental Details. Chromium telluride nanoplates were synthesized in a three-zone tube furnace *via* a CVD process. A schematic of the experimental setup and growth details are provided in the Supporting Information. The morphology, chemical composition, and thickness of the chromium telluride nanoplates were characterized by optical microscopy (Olympus BX51M), scanning electron microscopy (SEM, FEI Quanta 600F), and atomic force microscopy (AFM, Asylum Research MFP-3D). The X-ray diffraction (XRD) $2\theta-\theta$ patterns of two samples were respectively measured in a Bruker D8 Discover system. A pair of slits with a width of 0.6 mm were used to define the beam width in order to improve the measurement accuracy. The crystalline structure of the nanoplates was studied by TEM images, and SAED patterns were acquired using a JEOL 3200FS operated at 300 kV. Magnetization measurements were carried out using a Quantum Design superconducting quantum interference diffractometer (SQUID). In the MOKE measurements, the sample was mounted inside a Montana Instrument Cryostation, where a single-pole homemade electromagnet provided an out-of-plane magnetic field in the range of −600 Oe and +600 Oe. The light source was a He−Ne laser (λ = 633 nm), with a power of 25 μW and an estimated beam size of 10 μm. The incident beam is p-polarized with a small incident angle of about 5°. Kerr rotation imparted on the reflection beam was analyzed with a half waveplate, Wollaston beam splitter, and a balanced photodiode bridge [Figure S13]. The incident beam intensity was modulated with a mechanical chopper at a frequency around 1 kHz, and a lock-in amplifier was locked to the same frequency in detecting the signal from the balanced photodiode bridge.

Calculation Details. The magnetic structure of Cr_2Te_3 was studied by using DFT. The calculations were conducted with VASP.[89] In this study, the GGA approach was employed,[90] and the pseudopotentials were generated with the PAW method.[91] The exchange−-correlation density functional was expressed by the PBE.[92] The HSE06 functional was used to perform screened hybrid functional calculations.[93,94] The experimental lattice parameters (a = 6.829 Å and c = 11.922 Å at 4.2 K[57]) were adopted for the

https://dx.doi.org/10.1021/acsnano.0c05534
ACS Nano 2020, 14, 15256−15266

calculations. The screening parameter μ was set to 0.2 E^{-1}. The cutoff energy of the plane wave basis set was 500 eV. During the hybrid functional calculations, the first Brillouin zone was sampled by a 5 × 5 × 3 k point grid generated by a Monkhorst−Pack scheme. For GGA calculations, a 11 × 11 × 5 Monkhorst−Pack grid was employed. The tetrahedron method with Blöchl corrections was employed in the calculations. When calculating the magnetic anisotropy constant and the energy difference between the FM state and the FIM state, the convergence criterion for the calculations was 10^{-8} eV. The energies were calculated using hybrid functional and GGA+U methods with different U values. By comparing these energies, the value of U was determined to be 1.7 eV for other calculations. By using GGA+U with U = 1.7 eV, the noncollinear calculations of canted states were conducted. They converged when the energy change between steps was smaller than 10^{-6} eV, and the angle changes and magnitude changes of each local magnetic moment were smaller than 0.5° and 0.01 μ_b for five steps.

ASSOCIATED CONTENT

Supporting Information

The Supporting Information is available free of charge at https://pubs.acs.org/doi/10.1021/acsnano.0c05534.

Experimental details of the synthesis and schematic of three-zone tube furnace; optical images of the Cr_2Te_3 nanoplates after being transferred *via* stamping; XRD scans of the Cr_2Te_3 samples and Cr_2Te_3 and Cr_5Te_8 XRD scans from PDFs; schematic unit cells and simulated diffraction patterns of various chromium tellurides; TEM-EDX spectra and elemental mappings of Cr and Te; preparation of samples for magnetization measurements; representative AFM scan of the samples; $M-H$ background subtraction and coercive field calculation; $M-H$ data of the thick sample at 3 K; experimental MOKE setup and geometry; additional DFT results (PDF)

AUTHOR INFORMATION

Corresponding Author

Shixiong Zhang − *Department of Physics and Quantum Science and Engineering Center, Indiana University, Bloomington, Indiana 47405, United States; Department of Materials Science and NanoEngineering, Rice University, Houston, Texas 77005, United States;* orcid.org/0000-0002-1004-0597; Email: sxzhang@indiana.edu

Authors

Amanda L. Coughlin − *Department of Physics, Indiana University, Bloomington, Indiana 47405, United States*

Dongyue Xie − *Department of Mechanical and Materials Engineering, University of Nebraska, Lincoln, Nebraska 68588, United States*

Yue Yao − *Department of Physics and Astronomy, University of Utah, Salt Lake City, Utah 84112, United States*

Xun Zhan − *Electron Microscope Center, Indiana University, Bloomington, Indiana 47405, United States*

Qiang Chen − *Department of Physics and Astronomy, University of Tennessee, Knoxville, Tennessee 37996, United States*

Heshan Hewa-Walpitage − *Department of Physics and Astronomy, University of Utah, Salt Lake City, Utah 84112, United States*

Xiaohang Zhang − *Center for Nanophysics & Advanced Materials, University of Maryland, College Park, Maryland 20742, United States*

Hua Guo − *Department of Materials Science and NanoEngineering, Rice University, Houston, Texas 77005, United States*

Haidong Zhou − *Department of Physics and Astronomy, University of Tennessee, Knoxville, Tennessee 37996, United States*

Jun Lou − *Department of Materials Science and NanoEngineering, Rice University, Houston, Texas 77005, United States;* orcid.org/0000-0002-4351-9561

Jian Wang − *Department of Mechanical and Materials Engineering, University of Nebraska, Lincoln, Nebraska 68588, United States*

Yan S. Li − *Department of Physics and Astronomy, University of Utah, Salt Lake City, Utah 84112, United States*

Herbert A. Fertig − *Department of Physics and Quantum Science and Engineering Center, Indiana University, Bloomington, Indiana 47405, United States*

Complete contact information is available at: https://pubs.acs.org/10.1021/acsnano.0c05534

Notes

The authors declare no competing financial interest.

ACKNOWLEDGMENTS

We thank Dr. J. Zhang and Prof. R. Pynn for helpful discussions. S.X.Z. and H.A.F. acknowledge support by the National Science Foundation *via* grant no. ECCS-1936406. Q.C. and H.Z. thank the support from NSF-DMR-1350002. This work was supported in part by the NSF DMR-1506460 and DMR-1914451. H.A.F. acknowledges the support of the Research Corporation for Science Advancement through a Cottrell SEED Award and the US-Israel Binational Science Foundation through award No. 2016130. H.G. and J.L. gratefully acknowledge the support by the Welch grant C-1716 and the NSF I/UCRC Center for Atomically Thin Multifunctional Coatings (ATOMIC) under award # IIP-1539999. We thank the Indiana University−Bloomington Nanoscale Characterization Facility for access to the scanning electron microscope and atomic force microscope and the Electron Microscopy Center for the access to transmission electron microscopes. The atomistic simulations were completed utilizing the Holland Computing Center of the University of Nebraska, which receives support from the Nebraska Research Initiative.

REFERENCES

(1) Onsager, L. Crystal Statistics. I. A Two-Dimensional Model with an Order-Disorder Transition. *Phys. Rev.* **1944**, *65*, 117.

(2) Elmers, H.; Liu, G.; Gradmann, U. Magnetometry of the Ferromagnetic Monolayer Fe (110) on W (110) Coated with Ag. *Phys. Rev. Lett.* **1989**, *63*, 566.

(3) Lugert, G.; Bayreuther, G. Evidence for Perpendicular Magnetic Anisotropy in Fe (110) Epitaxial Films in the Monolayer Range on Gold. *Thin Solid Films* **1989**, *175*, 311−316.

(4) Rau, C. Ferromagnetic Order and Critical Behavior at Surfaces of Ultrathin Epitaxial Films. *Appl. Phys. A: Solids Surf.* **1989**, *49*, 579−587.

(5) Bland, J.; Bateson, R.; Heinrich, B.; Celinski, Z.; Lauter, H. Spin Polarised Neutron Reflection Studies of Ultrathin Magnetic Films. *J. Magn. Magn. Mater.* **1992**, *104*, 1909−1912.

(6) Gong, C.; Li, L.; Li, Z.; Ji, H.; Stern, A.; Xia, Y.; Cao, T.; Bao, W.; Wang, C.; Wang, Y.; Qiu, Z. Q.; Cava, R. J.; Louie, S. G.; Xia, J.; Zhang, X. Discovery of Intrinsic Ferromagnetism in Two-Dimensional Van Der Waals Crystals. *Nature* **2017**, *546*, 265−269.

(7) Huang, B.; Clark, G.; Navarro-Moratalla, E.; Klein, D. R.; Cheng, R.; Seyler, K. L.; Zhong, D.; Schmidgall, E.; McGuire, M. A.; Cobden, D. H.; Yao, W.; Xiao, D.; Jarillo-Herrero, P.; Xu, X. Layer-Dependent Ferromagnetism in a Van Der Waals Crystal Down to the Monolayer Limit. *Nature* **2017**, *546*, 270−273.
(8) Berezinsky, V. Destruction of Long Range Order in One-Dimensional and Two-Dimensional Systems Having a Continuous Symmetry Group. I. Classical Systems. *Zh. Eksp. Teor. Fiz.* **1970**, *32*, 493−500.
(9) Kosterlitz, J. M.; Thouless, D. J. Ordering, Metastability and Phase Transitions in Two-Dimensional Systems. *J. Phys. C: Solid State Phys.* **1973**, *6*, 1181.
(10) Mermin, N. D.; Wagner, H. Absence of Ferromagnetism or Antiferromagnetism in One-or Two-Dimensional Isotropic Heisenberg Models. *Phys. Rev. Lett.* **1966**, *17*, 1133.
(11) Burch, K. S.; Mandrus, D.; Park, J.-G. Magnetism in Two-Dimensional Van Der Waals Materials. *Nature* **2018**, *563*, 47−52.
(12) Zheng, F.; Zhao, J.; Liu, Z.; Li, M.; Zhou, M.; Zhang, S.; Zhang, P. Tunable Spin States in the Two-Dimensional Magnet Cri 3. *Nanoscale* **2018**, *10*, 14298−14303.
(13) Webster, L.; Yan, J.-A. Strain-Tunable Magnetic Anisotropy in Monolayer Crcl 3, Crbr 3, and Cri 3. *Phys. Rev. B: Condens. Matter Mater. Phys.* **2018**, *98*, 144411.
(14) Wu, Z.; Yu, J.; Yuan, S. Strain-Tunable Magnetic and Electronic Properties of Monolayer Cri 3. *Phys. Chem. Chem. Phys.* **2019**, *21*, 7750−7755.
(15) Song, T.; Cai, X.; Tu, M. W.-Y.; Zhang, X.; Huang, B.; Wilson, N. P.; Seyler, K. L.; Zhu, L.; Taniguchi, T.; Watanabe, K.; McGuire, M. A.; Cobden, D. H.; Xiao, D.; Yao, W.; Xu, X. Giant Tunneling Magnetoresistance in Spin-Filter Van Der Waals Heterostructures. *Science* **2018**, *360*, 1214−1218.
(16) Klein, D. R.; MacNeill, D.; Lado, J. L.; Soriano, D.; Navarro-Moratalla, E.; Watanabe, K.; Taniguchi, T.; Manni, S.; Canfield, P.; Fernández-Rossier, J.; Jarillo-Herrero, P. Probing Magnetism in 2d Van Der Waals Crystalline Insulators *via* Electron Tunneling. *Science* **2018**, *360*, 1218−1222.
(17) Wang, Z.; Gutiérrez-Lezama, I.; Ubrig, N.; Kroner, M.; Gibertini, M.; Taniguchi, T.; Watanabe, K.; Imamoğlu, A.; Giannini, E.; Morpurgo, A. F. Very Large Tunneling Magnetoresistance in Layered Magnetic Semiconductor Cri 3. *Nat. Commun.* **2018**, *9*, 1−8.
(18) Kim, H. H.; Yang, B.; Patel, T.; Sfigakis, F.; Li, C.; Tian, S.; Lei, H.; Tsen, A. W. One Million Percent Tunnel Magnetoresistance in a Magnetic Van Der Waals Heterostructure. *Nano Lett.* **2018**, *18*, 4885−4890.
(19) Zhong, D.; Seyler, K. L.; Linpeng, X.; Cheng, R.; Sivadas, N.; Huang, B.; Schmidgall, E.; Taniguchi, T.; Watanabe, K.; McGuire, M. A.; Yao, W.; Xiao, D.; Fu, K.-M. C.; Xu, X. Van Der Waals Engineering of Ferromagnetic Semiconductor Heterostructures for Spin and Valleytronics. *Sci. Adv.* **2017**, *3*, No. e1603113.
(20) Seyler, K. L.; Zhong, D.; Huang, B.; Linpeng, X.; Wilson, N. P.; Taniguchi, T.; Watanabe, K.; Yao, W.; Xiao, D.; McGuire, M. A.; Fu, K.-M. C.; Xu, X. Valley Manipulation by Optically Tuning the Magnetic Proximity Effect in Wse2/Cri3 Heterostructures. *Nano Lett.* **2018**, *18*, 3823−3828.
(21) Jiang, S.; Li, L.; Wang, Z.; Mak, K. F.; Shan, J. Controlling Magnetism in 2d Cri 3 by Electrostatic Doping. *Nat. Nanotechnol.* **2018**, *13*, 549−553.
(22) Wang, Z.; Zhang, T.; Ding, M.; Dong, B.; Li, Y.; Chen, M.; Li, X.; Huang, J.; Wang, H.; Zhao, X.; Li, Y.; Li, D.; Jia, C.; Sun, L.; Guo, H.; Ye, Y.; Sun, D.; Chen, Y.; Yang, T.; Zhang, J.; et al. Electric-Field Control of Magnetism in a Few-Layered Van Der Waals Ferromagnetic Semiconductor. *Nat. Nanotechnol.* **2018**, *13*, 554−559.
(23) Williams, T. J.; Aczel, A. A.; Lumsden, M. D.; Nagler, S. E.; Stone, M. B.; Yan, J.-Q.; Mandrus, D. Magnetic Correlations in the Quasi-Two-Dimensional Semiconducting Ferromagnet Crsite 3. *Phys. Rev. B: Condens. Matter Mater. Phys.* **2015**, *92*, 144404.
(24) Lee, J.-U.; Lee, S.; Ryoo, J. H.; Kang, S.; Kim, T. Y.; Kim, P.; Park, C.-H.; Park, J.-G.; Cheong, H. Ising-Type Magnetic Ordering in Atomically Thin Feps3. *Nano Lett.* **2016**, *16*, 7433−7438.
(25) Wang, X.; Du, K.; Liu, Y. Y. F.; Hu, P.; Zhang, J.; Zhang, Q.; Owen, M. H. S.; Lu, X.; Gan, C. K.; Sengupta, P. Raman Spectroscopy of Atomically Thin Two-Dimensional Magnetic Iron Phosphorus Trisulfide (Feps3). *2D Mater.* **2016**, *3*, 031009.
(26) Dong, S.; Liu, X.; Li, X.; Kanzyuba, V.; Yoo, T.; Rouvimov, S.; Vishwanath, S.; Xing, H. G.; Jena, D.; Dobrowolska, M.; Furdyna, J. K. Room Temperature Weak Ferromagnetism in Sn1− Xmnxse2 2d Films Grown by Molecular Beam Epitaxy. *APL Mater.* **2016**, *4*, 032601.
(27) Li, B.; Xing, T.; Zhong, M.; Huang, L.; Lei, N.; Zhang, J.; Li, J.; Wei, Z. A Two-Dimensional Fe-Doped Sns 2 Magnetic Semiconductor. *Nat. Commun.* **2017**, *8*, 1−7.
(28) Khan, I.; Hashmi, A.; Farooq, M. U.; Hong, J. Two-Dimensional Magnetic Semiconductor in Feroxyhyte. *ACS Appl. Mater. Interfaces* **2017**, *9*, 35368−35375.
(29) Yamasaki, Y.; Moriya, R.; Arai, M.; Masubuchi, S.; Pyon, S.; Tamegai, T.; Ueno, K.; Machida, T. Exfoliation and Van Der Waals Heterostructure Assembly of Intercalated Ferromagnet Cr1/3tas2. *2D Mater.* **2017**, *4*, 041007.
(30) Lee, J.; Ko, T. Y.; Kim, J. H.; Bark, H.; Kang, B.; Jung, S.-G.; Park, T.; Lee, Z.; Ryu, S.; Lee, C. Structural and Optical Properties of Single-and Few-Layer Magnetic Semiconductor Crps4. *ACS Nano* **2017**, *11*, 10935−10944.
(31) O'Hara, D. J.; Zhu, T.; Trout, A. H.; Ahmed, A. S.; Luo, Y. K.; Lee, C. H.; Brenner, M. R.; Rajan, S.; Gupta, J. A.; McComb, D. W.; Kawakami, R. K. Room Temperature Intrinsic Ferromagnetism in Epitaxial Manganese Selenide Films in the Monolayer Limit. *Nano Lett.* **2018**, *18*, 3125−3131.
(32) Bonilla, M.; Kolekar, S.; Ma, Y.; Diaz, H. C.; Kalappattil, V.; Das, R.; Eggers, T.; Gutierrez, H. R.; Phan, M.-H.; Batzill, M. Strong Room-Temperature Ferromagnetism in Vse 2 Monolayers on Van Der Waals Substrates. *Nat. Nanotechnol.* **2018**, *13*, 289−293.
(33) Fei, Z.; Huang, B.; Malinowski, P.; Wang, W.; Song, T.; Sanchez, J.; Yao, W.; Xiao, D.; Zhu, X.; May, A. F.; Wu, W.; Cobden, D. H.; Chu, J.-H.; Xu, X. Two-Dimensional Itinerant Ferromagnetism in Atomically Thin Fe 3 Gete 2. *Nat. Mater.* **2018**, *17*, 778−782.
(34) Shabbir, B.; Nadeem, M.; Dai, Z.; Fuhrer, M. S.; Xue, Q.-K.; Wang, X.; Bao, Q. Long Range Intrinsic Ferromagnetism in Two Dimensional Materials and Dissipationless Future Technologies. *Appl. Phys. Rev.* **2018**, *5*, 041105.
(35) Deng, Y.; Yu, Y.; Song, Y.; Zhang, J.; Wang, N. Z.; Sun, Z.; Yi, Y.; Wu, Y. Z.; Wu, S.; Zhu, J.; Wang, J.; Chen, X. H.; Zhang, Y. Gate-Tunable Room-Temperature Ferromagnetism in Two-Dimensional Fe 3 Gete 2. *Nature* **2018**, *563*, 94−99.
(36) Tokmachev, A. M.; Averyanov, D. V.; Parfenov, O. E.; Taldenkov, A. N.; Karateev, I. A.; Sokolov, I. S.; Kondratev, O. A.; Storchak, V. G. Emerging Two-Dimensional Ferromagnetism in Silicene Materials. *Nat. Commun.* **2018**, *9*, 1−9.
(37) Tan, C.; Lee, J.; Jung, S.-G.; Park, T.; Albarakati, S.; Partridge, J.; Field, M. R.; McCulloch, D. G.; Wang, L.; Lee, C. Hard Magnetic Properties in Nanoflake Van Der Waals Fe 3 Gete 2. *Nat. Commun.* **2018**, *9*, 1−7.
(38) Ma, Y.; Chinchore, A. V.; Smith, A. R.; Barral, M. A.; Ferrari, V. A Two-Dimensional Manganese Gallium Nitride Surface Structure Showing Ferromagnetism at Room Temperature. *Nano Lett.* **2018**, *18*, 158−166.
(39) Li, Q.; Yang, M.; Gong, C.; Chopdekar, R. V.; N'Diaye, A. T.; Turner, J.; Chen, G.; Scholl, A.; Shafer, P.; Arenholz, E.; Schmid, A. K.; Wang, S.; Liu, K.; Gao, N.; Admasu, A. S.; Cheong, S.-W.; Hwang, C.; Li, J.; Wang, F.; Zhang, X.; et al. Patterning-Induced Ferromagnetism of Fe3gete2 Van Der Waals Materials Beyond Room Temperature. *Nano Lett.* **2018**, *18*, 5974−5980.
(40) Abramchuk, M.; Jaszewski, S.; Metz, K. R.; Osterhoudt, G. B.; Wang, Y.; Burch, K. S.; Tafti, F. Controlling Magnetic and Optical Properties of the Van Der Waals Crystal Crcl3− Xbrx *via* Mixed Halide Chemistry. *Adv. Mater.* **2018**, *30*, 1801325.
(41) Jiang, Z.; Wang, P.; Xing, J.; Jiang, X.; Zhao, J. Screening and Design of Novel 2d Ferromagnetic Materials with High Curie

https://dx.doi.org/10.1021/acsnano.0c05534
ACS Nano 2020, 14, 15256−15266

Temperature above Room Temperature. *ACS Appl. Mater. Interfaces* **2018**, *10*, 39032−39039.
(42) Frey, N. C.; Kumar, H.; Anasori, B.; Gogotsi, Y.; Shenoy, V. B. Tuning Noncollinear Spin Structure and Anisotropy in Ferromagnetic Nitride Mxenes. *ACS Nano* **2018**, *12*, 6319−6325.
(43) Huang, C.; Feng, J.; Wu, F.; Ahmed, D.; Huang, B.; Xiang, H.; Deng, K.; Kan, E. Toward Intrinsic Room-Temperature Ferromagnetism in Two-Dimensional Semiconductors. *J. Am. Chem. Soc.* **2018**, *140*, 11519−11525.
(44) Qi, J.; Wang, H.; Qian, X. Electrically Tunable, High Curie Temperature 2d Ferromagnetism in Van Der Waals Layered Crystals. *Appl. Phys. Lett.* **2018**, *117*, 1−9.
(45) Yang, W.; Coughlin, A. L.; Webster, L.; Ye, G.; Lopez, K.; Fertig, H. A.; He, R.; Yan, J.-A.; Zhang, S. Highly Tunable Raman Scattering and Transport in Layered Magnetic Cr2s3 Nanoplates Grown by Sulfurization. *2D Mater.* **2019**, *6*, 035029.
(46) Zhang, W.; Zhang, L.; Wong, P. K. J.; Yuan, J.; Vinai, G.; Torelli, P.; van der Laan, G.; Feng, Y. P.; Wee, A. T. Magnetic Transition in Monolayer Vse2 *via* Interface Hybridization. *ACS Nano* **2019**, *13*, 8997−9004.
(47) Zhang, T.; Wang, Y.; Li, H.; Zhong, F.; Shi, J.; Wu, M.; Sun, Z.; Shen, W.; Wei, B.; Hu, W.; Liu, X.; Huang, L.; Hu, C.; Wang, Z.; Jiang, C.; Yang, S.; Zhang, Q.-m.; Qu, Z. Magnetism and Optical Anisotropy in Van Der Waals Antiferromagnetic Insulator Crocl. *ACS Nano* **2019**, *13*, 11353−11362.
(48) Lohmann, M.; Su, T.; Niu, B.; Hou, Y.; Alghamdi, M.; Aldosary, M.; Xing, W.; Zhong, J.; Jia, S.; Han, W.; Wu, R.; Cui, Y.-T.; Shi, J. Probing Magnetism in Insulating Cr2ge2te6 by Induced Anomalous Hall Effect in Pt. *Nano Lett.* **2019**, *19*, 2397−2403.
(49) Pasco, C. M.; El Baggari, I.; Bianco, E.; Kourkoutis, L. F.; McQueen, T. M. Tunable Magnetic Transition to a Singlet Ground State in a 2d Van Der Waals Layered Trimerized Kagomé Magnet. *ACS Nano* **2019**, *13*, 9457−9463.
(50) Lee, D. J.; Lee, Y.; Kwon, Y. H.; Choi, S. H.; Yang, W.; Kim, D. Y.; Lee, S. Room-Temperature Ferromagnetic Ultrathin A-Moo3: Te Nanoflakes. *ACS Nano* **2019**, *13*, 8717−8724.
(51) Zhang, W.; Wong, P. K. J.; Zhou, X.; Rath, A.; Huang, Z.; Wang, H.; Morton, S. A.; Yuan, J.; Zhang, L.; Chua, R.; Zeng, S.; Liu, E.; Xu, F.; Ariando; Chua, D. H.; Feng, Y. P.; van der Laan, G.; Pennycook, S. J.; Zhai, Y.; Wee, A. T. Ferromagnet/Two-Dimensional Semiconducting Transition-Metal Dichalcogenide Interface with Perpendicular Magnetic Anisotropy. *ACS Nano* **2019**, *13*, 2253−2261.
(52) Cui, F.; Zhao, X.; Xu, J.; Tang, B.; Shang, Q.; Shi, J.; Huan, Y.; Liao, J.; Chen, Q.; Hou, Y.; Zhang, Q.; Pennycook, S. J.; Zhang, Y. Controlled Growth and Thickness-Dependent Conduction-Type Transition of 2d Ferrimagnetic Cr2s3 Semiconductors. *Adv. Mater.* **2020**, *32*, 1905896.
(53) Balan, A. P.; Radhakrishnan, S.; Woellner, C. F.; Sinha, S. K.; Deng, L.; de los Reyes, C.; Rao, B. M.; Paulose, M.; Neupane, R.; Apte, A.; Kochat, V.; Vajtai, R.; Harutyunyan, A. R.; Chu, C.-W.; Costin, G.; Galvao, D. S.; Martí, A. A.; van Aken, P. A.; Varghese, O. K.; Tiwary, C. S.; et al. Exfoliation of a Non-Van Der Waals Material from Iron Ore Hematite. *Nat. Nanotechnol.* **2018**, *13*, 602−609.
(54) Yuan, J.; Balk, A.; Guo, H.; Fang, Q.; Patel, S.; Zhao, X.; Terlier, T.; Natelson, D.; Crooker, S.; Lou, J. Room-Temperature Magnetic Order in Air-Stable Ultrathin Iron Oxide. *Nano Lett.* **2019**, *19*, 3777−3781.
(55) Niu, B.; Su, T.; Francisco, B. A.; Ghosh, S.; Kargar, F.; Huang, X.; Lohmann, M.; Li, J.; Xu, Y.; Taniguchi, T.; Watanabe, D. W.; Wu, D.; Balandin, A.; Shi, J.; Cui, Y.-T. Coexistence of Magnetic Orders in Two-Dimensional Magnet Cri3. *Nano Lett.* **2020**, *20*, 553−558.
(56) Li, S.; Ye, Z.; Luo, X.; Ye, G.; Kim, H. H.; Yang, B.; Tian, S.; Li, C.; Lei, H.; Tsen, A. W.; Sun, K.; He, R.; Zhao, L. Magnetic-Field-Induced Quantum Phase Transitions in a Van Der Waals Magnet. *Phys. Rev. X* **2020**, *10*, 011075.
(57) Andresen, A. F. Magnetic Structure of Cr2te3, Cr3te4, and Cr5te6. *Acta Chem. Scand.* **1970**, *24*, 3495−3509.
(58) Dijkstra, J.; Weitering, H.; Van Bruggen, C.; Haas, C.; De Groot, R. Band-Structure Calculations, and Magnetic and Transport Properties of Ferromagnetic Chromium Tellurides (Crte, Cr3te4, Cr2te3). *J. Phys.: Condens. Matter* **1989**, *1*, 9141.
(59) Hamasaki, T.; Hashimoto, T.; Yamaguchi, Y.; Watanabe, H. Neutron Diffraction Study of Cr2te3 Single Crystal. *Solid State Commun.* **1975**, *16*, 895−897.
(60) Ipser, H.; Komarek, K. L.; Klepp, K. O. Transition Metal-Chalcogen Systems Viii: The Cr— Te Phase Diagram. *J. Less-Common Met.* **1983**, *92*, 265−282.
(61) Bensch, W.; Helmer, O.; Näther, C. Determination and Redetermination of the Crystal Structures of Chromium Tellurides in the Composition Range Crte1. 56−Crte1. 67: Trigonal Di-Chromium Tri-Telluride Cr2te3, Monoclinic Penta-Chromium Octa-Telluride Cr5te8, and the Five Layer Superstructure of Trigonal Penta-Chromium Octa-Telluride Cr5te8. *Mater. Res. Bull.* **1997**, *32*, 305−318.
(62) Luo, X.-H.; Ren, W.-J.; Zhang, Z.-D. Magnetic Properties and Magnetocaloric Effect of a Trigonal Te-Rich Cr5te8 Single Crystal. *J. Magn. Magn. Mater.* **2018**, *445*, 37−43.
(63) Lukowski, M. A.; Daniel, A. S.; Meng, F.; Forticaux, A.; Li, L.; Jin, S. Enhanced Hydrogen Evolution Catalysis from Chemically Exfoliated Metallic Mos2 Nanosheets. *J. Am. Chem. Soc.* **2013**, *135*, 10274−10277.
(64) Lee, Y.-H.; Zhang, X.-Q.; Zhang, W.; Chang, M.-T.; Lin, C.-T.; Chang, K.-D.; Yu, Y.-C.; Wang, J. T.-W.; Chang, C.-S.; Li, L.-J.; Lin, T.-W. Synthesis of Large-Area MoS_2 Atomic Layers with Chemical Vapor Deposition. *Adv. Mater.* **2012**, *24*, 2320−2325.
(65) Liu, K. K.; Zhang, W.; Lee, Y. H.; Lin, Y. C.; Chang, M. T.; Su, C. Y.; Chang, C. S.; Li, H.; Shi, Y.; Zhang, H.; Lai, C. S.; Li, L. J. Growth of Large-Area and Highly Crystalline Mos2 Thin Layers on Insulating Substrates. *Nano Lett.* **2012**, *12*, 1538−1544.
(66) Li, Z.; Xu, E.; Losovyj, Y.; Li, N.; Chen, A.; Swartzentruber, B.; Sinitsyn, N.; Yoo, J.; Jia, Q.; Zhang, S. Surface Oxidation and Thermoelectric Properties of Indium-Doped Tin Telluride Nanowires. *Nanoscale* **2017**, *9*, 13014−13024.
(67) Neudachina, V. S.; Shatalova, T. B.; Shtanov, V. I.; Yashina, L. V.; Zyubina, T. S.; Tamm, M. E.; Kobeleva, S. P. Xps Study of Snte(100) Oxidation by Molecular Oxygen. *Surf. Sci.* **2005**, *584*, 77−82.
(68) Wu, Z.; Liang, G.; Pang, W. K.; Zhou, T.; Cheng, Z.; Zhang, W.; Liu, Y.; Johannessen, B.; Guo, Z. Coupling Topological Insulator Snsb2te4 Nanodots with Highly Doped Graphene for High-Rate Energy Storage. *Adv. Mater.* **2020**, *32*, 1905632.
(69) Burn, D. M.; Duffy, L.; Fujita, R.; Zhang, S.; Figueroa, A. I.; Herrero-Martin, J.; Van Der Laan, G.; Hesjedal, T. Cr 2 Te 3 Thin Films for Integration in Magnetic Topological Insulator Heterostructures. *Sci. Rep.* **2019**, *9*, 1−10.
(70) Abraham, D. W.; Frank, M. M.; Guha, S. Absence of Magnetism in Hafnium Oxide Films. *Appl. Phys. Lett.* **2005**, *87*, 252502.
(71) Hashimoto, T.; Hoya, K.; Yamaguchi, M.; Ichitsubo, I. Magnetic Properties of Single Crystals Cr2-Δte3. *J. Phys. Soc. Jpn.* **1971**, *31*, 679−682.
(72) Roy, A.; Guchhait, S.; Dey, R.; Pramanik, T.; Hsieh, C.-C.; Rai, A.; Banerjee, S. K. Perpendicular Magnetic Anisotropy and Spin Glass-Like Behavior in Molecular Beam Epitaxy Grown Chromium Telluride Thin Films. *ACS Nano* **2015**, *9*, 3772−3779.
(73) Li, H.; Wang, L.; Chen, J.; Yu, T.; Zhou, L.; Qiu, Y.; He, H.; Ye, F.; Sou, I. K.; Wang, G. Molecular Beam Epitaxy Grown Cr2te3 Thin Films with Tunable Curie Temperatures for Spintronic Devices. *ACS Appl. Nano Mater.* **2019**, *2*, 6809−6817.
(74) Pramanik, T.; Roy, A.; Dey, R.; Rai, A.; Guchhait, S.; Movva, H. C.; Hsieh, C.-C.; Banerjee, S. K. Angular Dependence of Magnetization Reversal in Epitaxial Chromium Telluride Thin Films with Perpendicular Magnetic Anisotropy. *J. Magn. Magn. Mater.* **2017**, *437*, 72−77.
(75) During the preparation of our paper, we noticed a related paper: Wen, Y.; Liu, Z.; Zhang, Y.; Xia, C.; Zhai, B.; Zhang, X.; Zhai,

https://dx.doi.org/10.1021/acsnano.0c05534
ACS Nano 2020, 14, 15256−15266

G.; Shen, C.; He, P.; Cheng, R.; Yin, L.; Yao, Y.; Sendeku, M. G.; Wang, Z.; Ye, X.; Liu, C.; Jiang, C.; Shan, C.; Long, Y.; He, J. Tunable Room-Temperature Ferromagnetism in Two-Dimensional Cr2te3. *Nano Lett.* **2020**, *20*, 3130−3139.
(76) Cullity, B. D.; Graham, C. D. *Introduction to Magnetic Materials*; John Wiley & Sons: New York, 2011; pp 218−226.
(77) Wang, F.; Du, J.; Sun, F.; Sabirianov, R. F.; Al-Aqtash, N.; Sengupta, D.; Zeng, H.; Xu, X. Ferromagnetic Cr2Te3 Nanorods with Ultrahigh Coercivity. *Nanoscale* **2018**, *10*, 11028−11033.
(78) Youn, S.; Kwon, S.; Min, B. Correlation Effect and Magnetic Moments in Cr 2 Te 3. *J. Appl. Phys.* **2007**, *101*, 09G522.
(79) Zhang, X.; Zhao, Y.; Song, Q.; Jia, S.; Shi, J.; Han, W. Magnetic Anisotropy of the Single-Crystalline Ferromagnetic Insulator Cr2ge2te6. *Jpn. J. Appl. Phys.* **2016**, *55*, 033001.
(80) Richter, N.; Weber, D.; Martin, F.; Singh, N.; Schwingenschlögl, U.; Lotsch, B. V.; Kläui, M. Temperature-Dependent Magnetic Anisotropy in the Layered Magnetic Semiconductors Cr I 3 and Crb R 3. *Phys, Rev. Mater.* **2018**, *2*, 024004.
(81) Néel, L. Anisotropie Magnétique Superficielle Et Surstructures D'orientation. *J. Phys. Radium* **1954**, *15*, 225−239.
(82) Gradmann, U. Ferromagnetism near Surfaces and in Thin Films. *Appl. Phys.* **1974**, *3*, 161−178.
(83) Binns, C. Chapter 9: Magnetism at Surfaces and Interfaces. In *Handbook of Surfaces and Interfaces of Materials*, Nalwa, H. S., Ed.; Academic Press: Burlington, 2001; pp 357−392.
(84) Gradmann, U.; Müller, J. Flat Ferromagnetic, Epitaxial 48ni/52fe (111) Films of Few Atomic Layers. *Phys. Status Solidi B* **1968**, *27*, 313−324.
(85) Pappas, D.; Kämper, K.-P.; Hopster, H. Reversible Transition between Perpendicular and in-Plane Magnetization in Ultrathin Films. *Phys. Rev. Lett.* **1990**, *64*, 3179.
(86) Qiu, Z.; Pearson, J.; Bader, S. Asymmetry of the Spin Reorientation Transition in Ultrathin Fe Films and Wedges Grown on Ag (100). *Phys. Rev. Lett.* **1993**, *70*, 1006.
(87) Bruno, P. Magnetization and Curie Temperature of Ferromagnetic Ultrathin Films: The Influence of Magnetic Anisotropy and Dipolar Interactions. *MRS Online Proc. Libr.* **1991**, *231*, 299−310.
(88) Zhang, L.-Z.; He, X.-D.; Zhang, A.-L.; Xiao, Q.-L.; Lu, W.-L.; Chen, F.; Feng, Z.; Cao, S.; Zhang, J.; Ge, J.-Y. Tunable Curie Temperature in Layered Ferromagnetic Cr5+ X Te8 Single Crystals. *APL Mater.* **2020**, *8*, 031101.
(89) Kresse, G.; Joubert, D. From Ultrasoft Pseudopotentials to the Projector Augmented-Wave Method. *Phys. Rev. B: Condens. Matter Mater. Phys.* **1999**, *59*, 1758.
(90) Perdew, J. P.; Chevary, J. A.; Vosko, S. H.; Jackson, K. A.; Pederson, M. R.; Singh, D. J.; Fiolhais, C. Atoms, Molecules, Solids, and Surfaces: Applications of the Generalized Gradient Approximation for Exchange and Correlation. *Phys. Rev. B: Condens. Matter Mater. Phys.* **1992**, *46*, 6671.
(91) Blöchl, P. E. Projector Augmented-Wave Method. *Phys. Rev. B: Condens. Matter Mater. Phys.* **1994**, *50*, 17953.
(92) Perdew, J. P.; Burke, K.; Ernzerhof, M. Generalized Gradient Approximation Made Simple. *Phys. Rev. Lett.* **1996**, *77*, 3865.
(93) Heyd, J.; Scuseria, G. E.; Ernzerhof, M. Hybrid Functionals Based on a Screened Coulomb Potential. *J. Chem. Phys.* **2003**, *118*, 8207−8215.
(94) Heyd, J.; Scuseria, G. E.; Ernzerhof, M. Erratum:"Hybrid Functionals Based on a Screened Coulomb Potential"[J. Chem. Phys. 118, 8207 (2003)]. *J. Chem. Phys.* **2006**, *124*, 219906.
(95) Lin, Z.; Lohmann, M.; Ali, Z. A.; Tang, C.; Li, J.; Xing, W.; Zhong, J.; Jia, S.; Han, W.; Coh, S.; Beyermann, W.; Shi, J. Pressure-Induced Spin Reorientation Transition in Layered Ferromagnetic Insulator Cr 2 Ge 2 Te 6. *Phys, Rev. Mater.* **2018**, *2*, 051004.
(96) Fang, Y.; Wu, S.; Zhu, Z.-Z.; Guo, G.-Y. Large Magneto-Optical Effects and Magnetic Anisotropy Energy in Two-Dimensional Cr 2 Ge 2 Te 6. *Phys. Rev. B: Condens. Matter Mater. Phys.* **2018**, *98*, 125416.
(97) Zhou, L.; Chen, J.; Chen, X.; Xi, B.; Qiu, Y.; Zhang, J.; Wang, L.; Zhang, R.; Ye, B.; Chen, P.; Zhang, X.; Guo, G.; Yu, D.; Mei, J.-W.; Ye, F.; Wang, G.; He, H. Topological Hall Effect in Bulk Ferromagnet Cr2te3 Embedded with Black-Phosphorus-Like Bismuth Nanosheets. *arXiv preprint arXiv:1903.06486* **2019**, 1−6.
(98) Chen, J.; Wang, L.; Zhang, M.; Zhou, L.; Zhang, R.; Jin, L.; Wang, X.; Qin, H.; Qiu, Y.; Mei, J. Evidence for Magnetic Skyrmions at the Interface of Ferromagnet/Topological-Insulator Heterostructures. *Nano Lett.* **2019**, *19*, 6144−6151.

https://dx.doi.org/10.1021/acsnano.0c05534
ACS Nano 2020, 14, 15256−15266